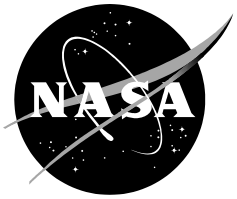
NASA/TM—20220005496



Application of Rotor Disk Model in the OVERFLOW CFD Code

Jasim U. Ahmad
Ames Research Center, Moffett Field, California

April 2022

NASA STI Program Report Series

The NASA STI Program collects, organizes, provides for archiving, and disseminates NASA's STI. The NASA STI program provides access to the NTRS Registered and its public interface, the NASA Technical Reports Server, thus providing one of the largest collections of aeronautical and space science STI in the world. Results are published in both non-NASA channels and by NASA in the NASA STI Report Series, which includes the following report types:

- TECHNICAL PUBLICATION. Reports of completed research or a major significant phase of research that present the results of NASA Programs and include extensive data or theoretical analysis. Includes compilations of significant scientific and technical data and information deemed to be of continuing reference value. NASA counterpart of peer-reviewed formal professional papers but has less stringent limitations on manuscript length and extent of graphic presentations.

- TECHNICAL MEMORANDUM. Scientific and technical findings that are preliminary or of specialized interest, e.g., quick release reports, working papers, and bibliographies that contain minimal annotation. Does not contain extensive analysis.

- CONTRACTOR REPORT. Scientific and technical findings by NASA-sponsored contractors and grantees.

- CONFERENCE PUBLICATION. Collected papers from scientific and technical conferences, symposia, seminars, or other meetings sponsored or co-sponsored by NASA.

- SPECIAL PUBLICATION. Scientific, technical, or historical information from NASA programs, projects, and missions, often concerned with subjects having substantial public interest.

- TECHNICAL TRANSLATION. English-language translations of foreign scientific and technical material pertinent to NASA's mission.

Specialized services also include organizing and publishing research results, distributing specialized research announcements and feeds, providing information desk and personal search support, and enabling data exchange services.

For more information about the NASA STI program, see the following:

- Access the NASA STI program home page at http://www.sti.nasa.gov

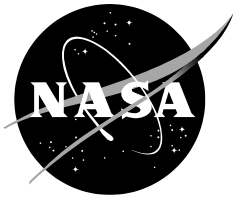
- Help desk contact information:

https://www.sti.nasa.gov/sti-contact-form/ and select the "General" help request type.

Acknowledgments

This report is available in electronic form at
http://

NASA/TM—20220005496



Application of Rotor Disk Model in the OVERFLOW CFD Code

Jasim U. Ahmad
Ames Research Center, Moffett Field, California

National Aeronautics and
Space Administration

Ames Research Center

April 2022

Abstract

To reduce the complexity and to reduce the cost of turnaround time of simulating unsteady flows of rotating blades with moving overset grids, a mid-fidelity option is provided in the OVERFLOW computational fluid dynamics analysis to model rotors and propellers as infinitely thin disks. The effect of the flow through the disk is represented by the momentum source terms in the governing Navier-Stokes equations. The model is loosely coupled with the rotorcraft comprehensive analysis CAMRADII. A brief description of the coupling algorithm is provided. Simulations of a single rotor and multiple rotors are shown, including comparisons with measurements and with the full rotor where all blades are modeled, and unsteady simulation performed with moving grids for rotating geometry.

Introduction

Helicopter flow fields are complex and require high-fidelity Navier-Stokes simulations for accurate representation. In general, the flow field of a conventional helicopter as well as multirotor vehicles, whether in forward flight or in hover, consist of unsteady aerodynamics with complex three-dimensional wakes dominated by the blade tip vortices. The wake also contains shear layers that are produced as the turbulent boundary layers detach from the blade surface. As the tip vortices advect, the vortex cores entrain part of the shear layer and as such the flow is inherently unsteady. To capture the rotor blade aerodynamic-structural interactions, high-fidelity Computational Fluid Dynamics (CFD) and Computational Structural dynamics (CSD) analyses are coupled to accurately model the helicopter flow field, rotor blade motion, and rotor trim. The computational simulation of such unsteady, moving and often deforming surfaces, is time consuming, difficult, and not practical for use as design tools. Recently, there has been increased interest in the aerodynamics of multirotor vehicles such as those proposed for the emerging urban air mobility market; vehicle geometries include quadcopters, side-by-side rotors, and lift plus cruise configurations. Modeling these multirotor configurations requires increased computational cost because of the geometric complexity, and the rotor-rotor interactions as well as rotor structure interactions. We explore reduced-order modeling for the rotor to provide an alternative to the fully modeled rotor with overset grids.

In the past, lower-order aerodynamic models often based on blade element theory (BET) associated with momentum theory (BEMT) were used with some success and some obvious inherent limitations. The BEMT-based methods are computationally efficient and provide reasonable estimations of rotor performance. Some aerodynamic phenomena are not captured accurately, however, limiting the scope of the BEMT approach. In this study, we consider the Navier-Stokes equations coupled with a BET-based model for the rotor. These BET and momentum theory algorithms are used in many simulations, including ref [1-5] to mention few. Rajagopalan et al. [3-4] did some of the pioneering work with Euler and Navier-Stokes equation in the actuator rotor disk model framework. The assumptions of replacing the rotor with a disk consisting of an infinite number of blades are well established. O'Brian [2] provided some very detailed computational procedures, including the inherent limitations and advantages of the BET model coupled with the CFD method. In our study, we started with the earlier work done by Chaffin and Berry [1] who used the technique with a source term-based algorithm in the Navier-Stokes equations. The algorithm of this actuator-like disk model was implemented in the widely used NASA flow solver OVERFLOW [6]. Instead of computing the pressure jump across the disk directly, a source term was added to the right-hand side of the Navier-Stokes equations. The source terms were calculated from the CFD coupled with the BET rotor model.

The method was further enhanced by loosely coupling with a CSD solver for the fluid-structure interaction and to achieve rotor trim and the rotor control settings. The CSD solver and the rotor trim are part of the widely used rotorcraft comprehensive code CAMRAD II [7]. Section 1 summarizes the computational model for the disk. The details of the computational algorithm are available in many previous works, including the primary algorithm by Chaffin and Berry [1] used for our study. In the present study, the BET model was coupled with OVERFLOW in an

overset grid context. The details of the computational grid with specific grid requirements for the rotor disk are given in section 2. The input parameters that are used for the rotor disk model, in addition to the main OVERFLOW inputs are also provided.

The loosely coupled methodology describing the interface between OVERFLOW and CAMRAD II [8] is discussed in Section 3. It also summarizes the important aspect of blade orientation and motions. The detailed transformations related to the blade element and various coordinate systems used are not repeated here. However, for the first time, an approach is presented that includes the elastic deformation provided by the CSD coupled algorithm. Airfoil tables and model are described in Section 4.

Finally, some validation cases are presented in Section 5, along with some representative results with single and multiple rotors that have been presented elsewhere [9-13] for forward flight and hover. Moreover, some qualitative results are presented in this report for multiple rotors of the Lift+Cruise VTOL Aircraft configuration. Lift+Cruise type of aircrafts are intended to represent a class of VTOL aircraft which have been developed recently [14-17] for manned and unmanned operation, taking advantage of distributed electric propulsion. CFD simulations are presented in this report for this vehicle in forward flight, hover, and climb. Section 6 summarizes the results of this report.

1. Computational Rotor Model

The helicopter flowfield was computed using the Navier-Stokes equations; however, the rotor flowfield used a reduced-order model using a series of approximations. The first level of approximation consisted of retaining an unsteady framework and projecting the actual blades onto a disk so that they act on the fluid as they rotate around the axis. For the helicopter problem, the unsteady formulation at least captures the first harmonic effect. A further simplification was based on a steady-state assumption whereby the disk area is filled with an infinite number of blades, and the force distribution is scaled according to the trim target. In this case, the unsteady description is lost, but computational costs are drastically reduced to one steady-state simulation. Rajagopalan and Lim [4] provided a detailed description of how the spinning blades are related to the fixed CFD grid points of the disk. Chuiton [5] provides a detailed description of three different models for the actuator disk: boundary condition on variables, boundary condition on fluxes, and source term. In all three models, the influence of the actuator disk is fed into the flowfield using an update at each time step. For the present study, a source term-based disk model ref [1-4] was used to model the rotor where the loads were time- and space-averaged. The source term was computed using the Blade Element Theory where the blade was represented with a series of 2-D blade sections. At each time step of the simulation procedure, at each elemental area on the rotor disk, an average of the flow properties was determined from the most recently computed Navier-Stokes solution of the flowfield. The source term was added to the Right-Hand Side (RHS) of the equation, as shown in Eq (1).

$$\frac{\partial U}{\partial t}+\frac{\partial F}{\partial x}+\frac{\partial G}{\partial y}+\frac{\partial H}{\partial z}=S \qquad (1)$$

$U=[\rho,\rho u,\rho v,\rho w,\rho E]^T$ are the vectors of conservative variables. F,G,H are the convective and diffusive flux tensors in x, y, z, S is the formal introduction of the source terms due to the actuator disk for force per unit area for the disk.

$$f=(f_x,f_y,f_z)$$
$$S=[0,f_x,f_y,f_z,(f\cdot v)]^T$$

The BET enables the computation of the blade loads by performing 2-D aerodynamic analysis at each blade sectional element where each element is subjected to the local flight conditions. In forward flight, the flow conditions vary for each combination of the radial and azimuthal locations of the segment. To generate respective flight conditions for each element,

the overall rotor flight conditions must be transformed from the inertial axes to the blade element axes. Knowing the blade element axes and local flight conditions, lift, drag and moment coefficients can be obtained from 2D airfoil look-up tables. The aerodynamic coefficients are calculated based on the look-up tables for the corresponding sectional angle of attack and Mach number. In case an airfoil table is not available, full-potential based idealized aerodynamic coefficients can be used for the source term. Since 2-D tables come from wind tunnel or various other sources, the user needs to be knowledgeable of potential Reynolds number effects. Once local forces are known, they can be transferred back to the inertial frame through a series of inverse transformations; the forces are then used as source terms in the computational model.

The effect of blade motions and deformations, namely pitching and flapping degrees of freedom were determined based on the rotor trim. Torsional deformations were not included in the simulation presented here, though the coupled interface has the option to include the torsion deformations, as shown in section (2.1) below. A simplified trim procedure for the target thrust and moment balance is available in OVERFLOW. The appropriate approach, however, is to loosely couple OVERFLOW to CAMRAD II. CAMRAD II is an aeromechanics analysis of rotorcraft along with its aerodynamics module and CSD module. It incorporates a combination of advanced technologies, including multibody dynamics, nonlinear finite elements, and rotorcraft aerodynamics. Figure 1 shows the iterative approach for the coupled computation.

The coupling also allows the method to be applicable to free air trim as well as to wind tunnel conditions. This loose coupling procedure is described in section 3. Currently, in the OVERFLOW code, the source term is implemented through a boundary condition specification. The source term, as shown in the equation (1) is computed on a boundary cell of the computational grid and the variables are computed on that cell or as the average of the state variables of a few adjacent cells. This reduces the effect of local maxima/minima on a cell layer due to the sudden impact of source terms.

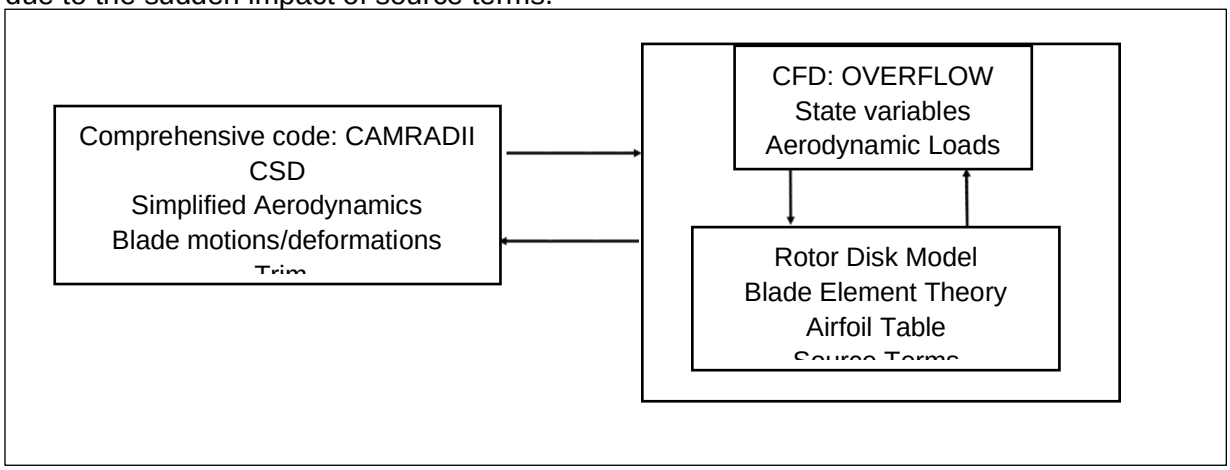


Figure 1: Schematic for CFD/CSD coupling for rotor disk model

2. Overset Grid System with Disk Model

The overset grid system used in the present simulations was generated using Chimera Grid Tools (CGT) software [18]. The CGT software contains a very efficient and modular grid scripting library used for grid manipulation, generation, reorganization, overset hole cutting surfaces, and generation of OVERFLOW input files. This scripting procedure produces high-quality surface grids and subsequent volume grids with a set of input parameters. These input parameters allow one to modify the grid system quickly and automatically for the existing geometry.

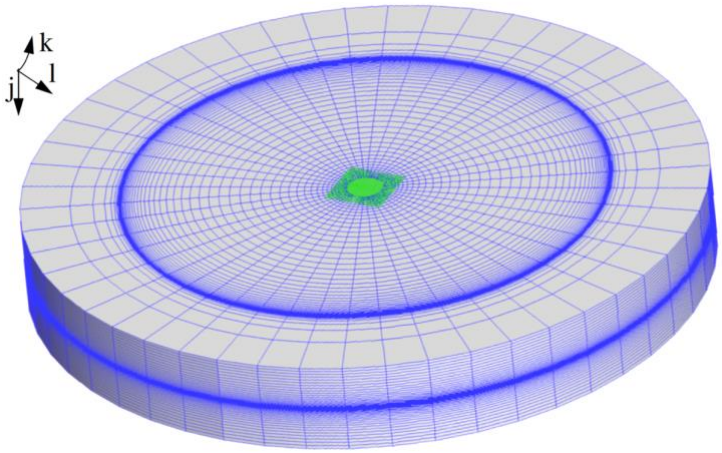


Figure 2. Disk grid along with block grid at the singular axis.

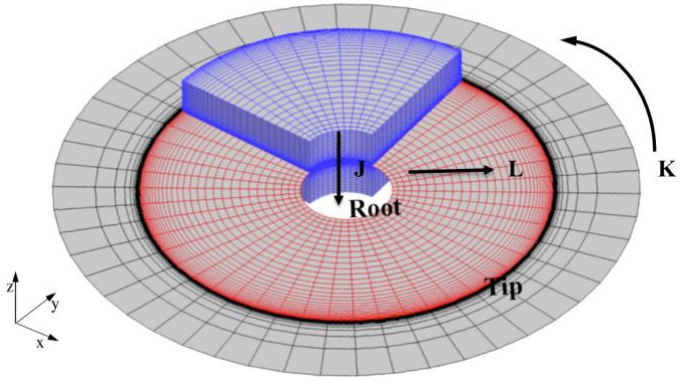


Figure 3. Disk grid cutout view showing the indices that needs to be specified for source term.

The disk model requires a cylindrical polar grid for convenience of source term grid transformation. A polar grid in conjunction with overset grid components is shown in Fig. 2. The singular axis of the grid is replaced with a block grid. The rotor disk model is implemented in specific grid indices. Fig. 3 shows a cutout view of the disk grid. The red portion of the grid represents the infinite number of rotor blades. Using the *jkl* convention, the plane of the disk should lie on a constant *j-plane*. The *j* direction is along the rotor shaft, with *j* increasing in the direction opposite of the thrust vector. This direction maintains a right-handed coordinate system and preserves the sign of the thrust coefficient. The *k* index wraps around the polar axis and is the periodic direction. The *l* direction increases along the blade span such that *l=1* is at the center of the disk and *l=lmax* is the outboard boundary. The rotor is located in between arbitrary *l* indices, based on the blade size, the inboard root tip, and the outboard blade tip. The source term is included in the simulation through the specification of a boundary condition.

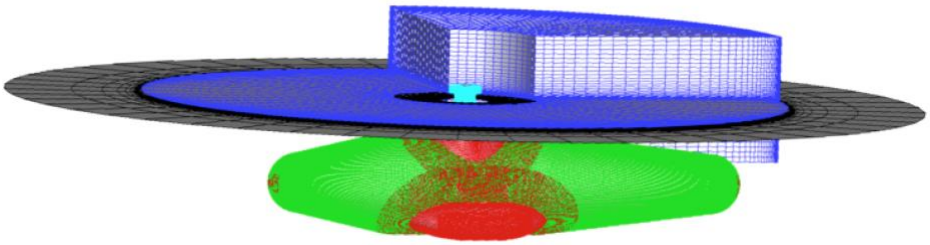


Figure 4. Disk grid together with fuselage and rotor hub.

Grid spacing should be compatible with the rest of the grid system, e.g., intergrid spacing does not exceed more than a factor 2. The singular axis in the polar grid is replaced with a block grid. These two grids are part of the “near-body” curvilinear overset grid system for an isolated rotor or a complete rotorcraft vehicle. These are imbedded into Cartesian “off-body” grids that resolve the rotor wake region and extend the computational domain to the farfield. These off-body Cartesian grids are automatically generated within OVERFLOW according to user specified input parameters. Moreover, the off-body Cartesian grids are generated at various levels of resolution starting from “Level 1” (L1) in the rotor-wake region, to successively coarser grid levels (L2, L3, L4…etc.) to extend the grid system rapidly and efficiently to the far field. Figure 4 shows a near-body grid system, which includes a fuselage and hub geometry in conjunction with the disk grid.

3. CFD/CSD Coupling and Trim

A ‘loose coupling' procedure for CFD and the comprehensive code is used for the rotor disk model. CAMRAD II is interfaced with OVERFLOW for full rotor unsteady simulation. In CAMRAD II, each rotor blade is structurally modeled. Beside CSD, CAMRAD II provides full helicopter trim capability. Similar to the full rotor simulation, the CFD load is transferred to CAMRAD II through interface module ‘delta load'. The delta load between CFD and CAMRAD II is used in correcting CAMRAD's aerodynamic load to compute new aerodynamic data and trim. Trim procedure is an important aspect of helicopter flight where the rotor loading accounts for a significant portion of the total vehicle forces and moments. The trim task finds the equilibrium solution for a steady-state operating condition and solves performance, loads, and vibration.

The CFD module in OVERFLOW for full rotor unsteady simulation uses individual blades with the moving body grids where the blade deformations from CAMRAD are given as (x, y, z) deflections of the quarter chord along with Euler-angle rotations, as a function of span and rotor azimuth angle. In the existing ‘loose coupling' setting, these quarter chord data are interfaced between CFD and comprehensive code through an interface tool of ‘motion module'. These quarter-chord data are used by the CFD code to define the three-dimensional blade surface at each time step. The deformed blades are then rotated through proper shaft azimuth angle to position each blade at the current instant of time. The deformations and Euler angles extracted from CAMRAD II solution are contained in the motion file which is the format used by CFD codes. These procedures are widely used after its first introduction by Potsdam, Yeo, and Johnson [8] with the OVERFLOW code.

Recently, OVERFLOW included an option of a rotor disk model beside full rotor simulation. Usage of CAMRAD II interface with rotor disk model and trim capability, however, were not attempted before. The concept of motion interface as discussed above is modified to accommodate the blade motions through control angles instead of quarter-chord displacement data. At some specified iterations step, the CFD provides the same loads as full rotor simulation to CAMRAD II through the ‘delta module' as described above and in turn, CAMRAD II provides the trimmed angles. This procedure is shown in Figure 5. The left side of the flow diagram shows the existing procedure for full rotor unsteady formulation while the right side shows the

new procedure for the rotor model. In a typical coupled simulation, the initial execution of the CFD code is carried out for one or two complete rotor revolutions, using blade deformations from a trimmed CAMRAD II solution with unmodified lifting-line (superscript LL Fig. 5) in aerodynamics. In subsequent coupling cycles, the flow solver is run for some n-blade multiple of revolution between coupling cycles (full revolution for some cases). At each coupling step, rotor loads from CFD are provided to CAMRAD II and in turn, CAMRAD II uses this CFD load to correct its lifting-line aerodynamics to retrim the rotor. At convergence, the CFD airloads fully replace comprehensive analysis airloads. The coupled OVERFLOW/CAMRAD II systems are tied together by separate interface tools that perform data translation between CFD and CSD.

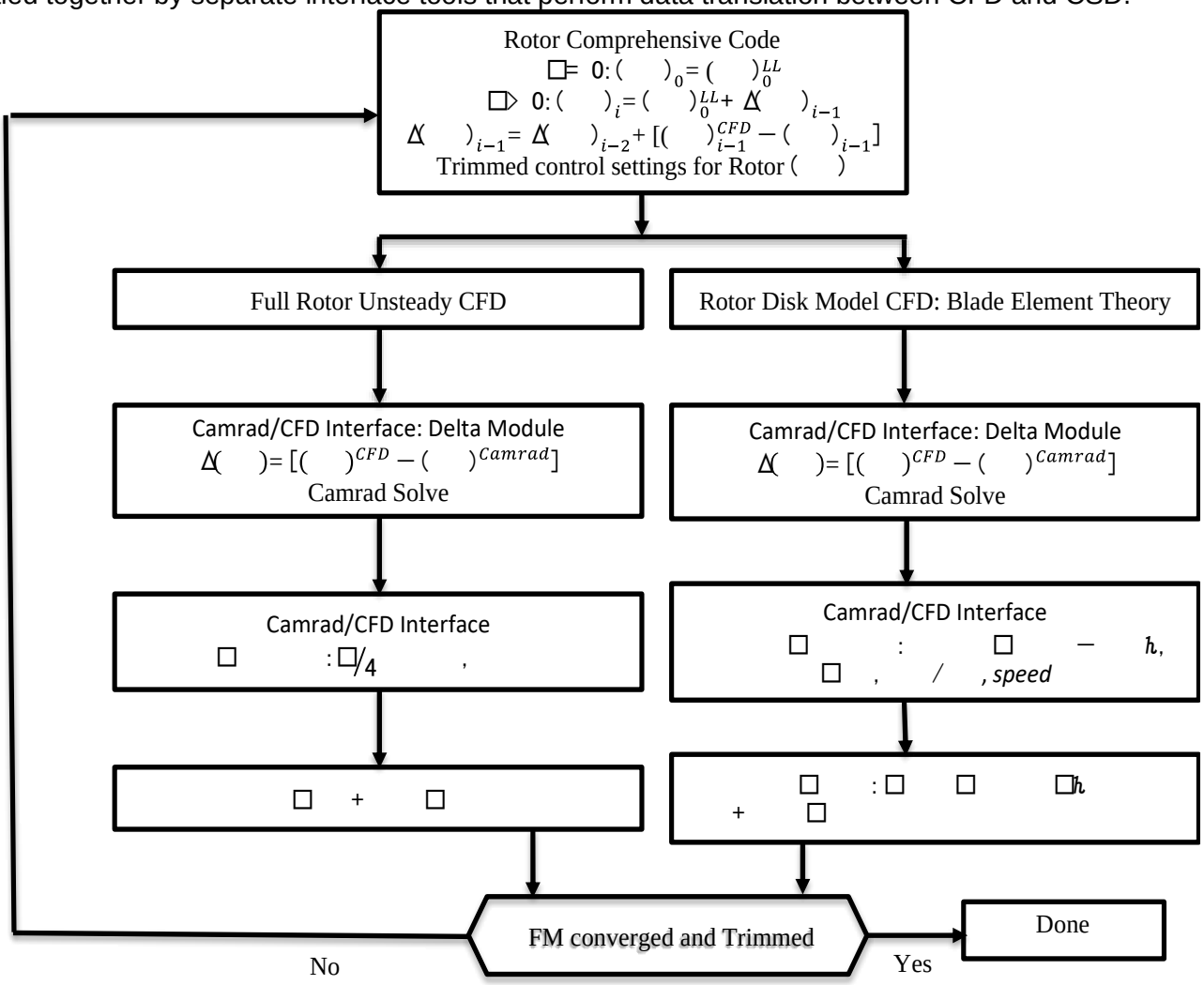


Figure 5. Loose coupling between CFD and CSD. The left side shows the full unsteady flow, the right side shows the disk model.

3.1 Blade Orientation and motion

The orientation and blade motion based on the CFD computed aerodynamic load is calculated by CAMRAD II. The trim update in CAMRAD II changes the pilot controls that require the orientation and motion to be recomputed periodically. For the disk model approach, that periodicity requirement is not needed and can be coupled at any arbitrary flow solutions steps in the OVERFLOW. The orientation of a blade section is determined through a series of coordinate system transformations. The orientation is defined by a set of unit vectors. The radial component points toward the blade tip, and the normal component points in the direction of the positive lift.

The chordwise component is determined such that the orientation vectors form a right-handed system. The direction of the chordwise component depends on the direction of the rotor rotation. For counterclockwise rotation, the chordwise vector points toward the leading edge of the blade and for clockwise rotation, the vector points toward the trailing edge.

The blade motions computed by CAMRAD II are interfaced with OVERFLOW through motion variables. The various blade angles, such as flapping, collective and cyclic control angles, and lead-lag angles are defined in motion variables that are used in computing the source terms in the flow solver. These angles used in computing blade element and rotor orientations are shown below. The lead-lag effects are not included here for now.

Blade feathering motion (considering only first harmonics) is given by

$$\theta = \theta_0 + \theta_{1s} sin\psi + \theta_{1c} cos\psi + \phi_\tau \quad (2)$$

ϕ_τ is the angle due to the torsional deformation.

Flapping motion of simple harmonics is written as

$$\beta = \beta_0 + \beta_{1s} sin\psi + \beta_{1c} cos\psi \quad (3)$$

The collective and cyclical motions are swashplate control for conventional helicopters. For non-conventional rotorcraft, such as small electrically powered fixed pitch multicopter vehicles, the thrust changes are achieved by changing the rotor speed using an Electrical Speed Controller (ESC). In the loosely coupled framework, the speed control prediction by CAMRAD II is implemented through the same motion variables as in the OVERFLOW code.

Figure 6 shows an idealized transformation of an articulated rotor for a typical helicopter. CAMRADII computes details of all the transformation of hinges and links. Following the hinge rotations, the orientation vectors are rotated by the blade azimuth angle. A series of transformations are needed for computing blade element forces and velocities that are related to the source term evaluation in computational or inertial frame $\{I_{cfd}: XYZ\}$. Attached to the rotor hub is the non-rotating hub plane coordinate $\{H: x^H y^H z^H\}$ and rotating hub frame $\{H_r: x^r y^r z^r\}$ and the blade element is attached to rotating frame $\{E: x^e y^e z^e\}$. The detailed description of these transformations can be found in many references [1-4, 7]. Instead here, the eqautions for various transformed components are given in Eq. (4-8). Equations (4) shows the velocity compoents in the non-rotating frame coordinate $\{H: x^H y^H z^H\}$. This equation as transformed to BET rotating frame $\{E: x^e y^e z^e\}$, is shown in Eq. (5-6). The induced angle and the effective angles of attack are shown in Eq. (7-8). Knowing local Mach number at {E}, and effective angles, lift and drags are computed using the airfoil tables. After computing blade element properties, namely $V \in \{E\}$ where $V \in \mathbb{R}^3$, inverse transformations are used to compute source terms $S \in \{XYZ\}$.

$$\boldsymbol{V}_{non-rotating} = [T]_I V_{cfd} \quad (4)$$

where $\boldsymbol{V}_{non-rotating}$ represent radial, tangential, and axial components, $[T]_{IH}$ is the transformation matrix.

The blade-fixed rotating components are given as:

$$\boldsymbol{V}_{BET} = [T]_H [T]_E \boldsymbol{V}_{non-rotating} \quad (5)$$

from which normal component is

$$v_n = v_{ncfd} - kr\dot{\beta} - v_r \sin\beta \quad (6)$$

here $k = 1$ for counterclockwise rotating rotor, $k = -1$ for clockwise rotating rotor.

These velocity components and angles are shown in a blade element diagram of Figure 7 for a forward flight. Induced angle φ is given as

$$\varphi = atan2(v_n, v_t) \quad (7)$$

v_t is the tangential component from eq. (5)

Effective angle of attack to be used with airfoil table is given by

$$\alpha_e = \theta + \varphi \quad (8)$$

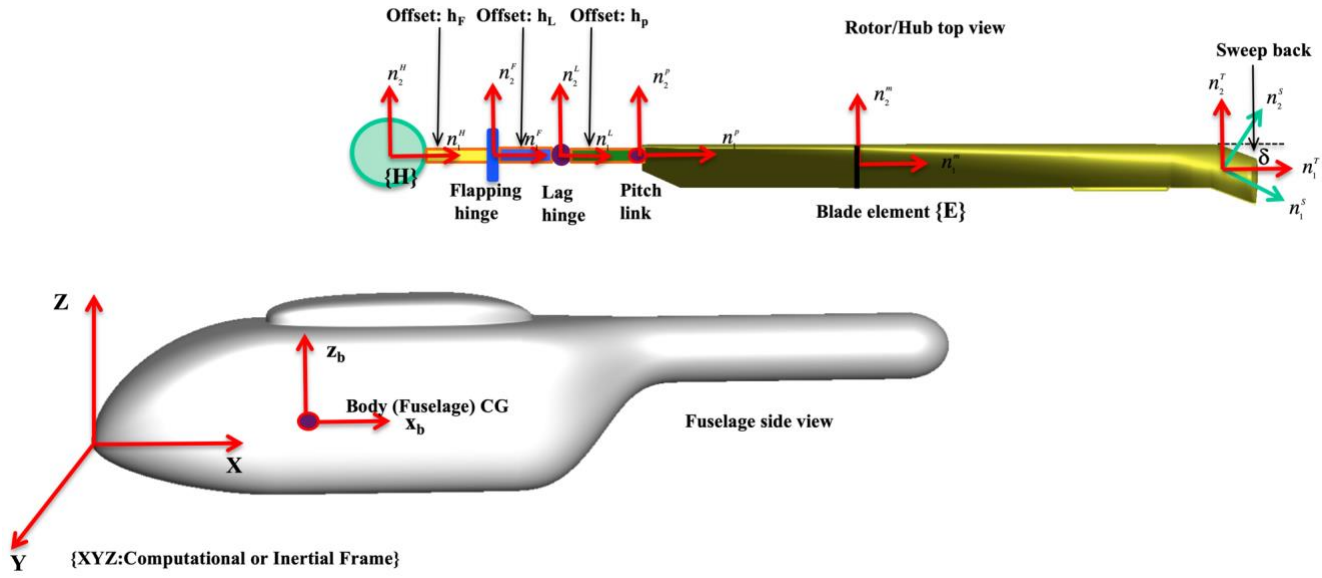


Figure 6. View of the various coordinate system. Rotor top view is enlarged

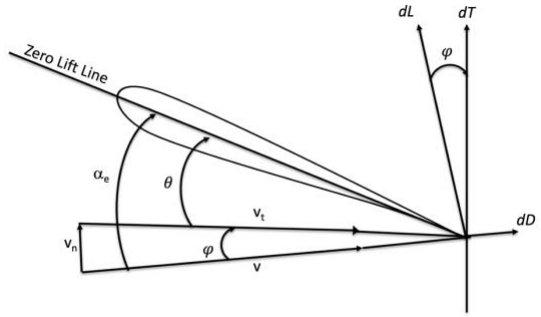


Figure 7. Blade element diagram for a forward flight.

4. Airfoil Table and Model

There are two approaches to determine the lift and drag of the blade elements. The first and widely used approach is to use airfoil tables arranged in the C81 format. Coefficients for airfoil lift, drag, and pitching moment are listed as a function of Mach number and angle-of-attack. This approach comes with the added expense of reading the table. A Fortran sample c81 table generation routine and table are given in Appendix A.

In lieu of airfoil tables, a second and simple approach is to model the lift and drag using a simple empirical model. This approach is given in OVERFLOW as an option for the disk model. This model assumes $c_l = 2\pi\alpha$. Stall is not modeled, but upper and lower limits are placed on the value of c_l. The user is given an option of using a Prandtl-Glauert Mach number correction, Kaplan's Rule correction, which also handles thickness effects, or no correction at all. The default is Prandtl-Glauert. These corrections primarily affect the slope of the lift curve. However, the maximum/minimum lift values should also decrease/increase as the Mach number increases. The values for drag are based on Hoerner's Fluid-Dynamic Drag and accounts for thickness and compressibility as well as drag divergence. Airfoils drag characteristics vary too much from one airfoil to the next to come up with a simple model.

5. Demonstration Results

A few demonstration calculations are included, together with validation and verification showing the convergence and effectiveness of the interface between CFD and CSD [10-17]. For

completeness, some results are repeated in this report. These results include a wide range of configurations from single to multiple rotors and from a conventional helicopter to UAM.

5. 1 Isolated rotor in Hover

An isolated rotor involving the XV-15 rotor is presented. The xv15 research vehicle data are widely used because of the publicly available existing wind tunnel and flight test. Felker and Betzina [9] provided the detailed performance data and documents for the outdoor hover tests at Ames Research Center. The experiment was conducted for a full-scale XV-15 isolated rotor in hover on the Outdoor Aerodynamic Research Facility (OARF) test bed. This free-air experiment does not have the wind tunnel wall effects, The present study compares the rotor performance data, Figure of Merit (FM). For comparison, thrust sweep of three data points were considered for a hover tip Mach = 0.69. Many previous simulations utilized this experimental data. The comprehensive code CAMRAD II [10] was used in analysis before. The present study used the CAMRAD II analysis data in performing a loosely coupled OVERFLOW's disk model simulation. Table 1 compares results for three trimmed thrust data points. The FM compares well. There is no specific trend in the data match. The two thrust cases slightly overpredict the FM, while the one thrust case underpredicts slightly.

CT/S	FM: Disk	FM: Experiment
0.1744	0.7184	0.7133
0.1351	0.7793	0.7854
0.1134	0.7896	0.7864

Table 3. xv15 in hover. Comparison of FM data to the experiment. Mtip = 0.69.

5. 2 UH-60A Rotor in Forward Flght

A simulation using the Navier-Stokes equations to determine the evolutionary and dynamical characteristics of the vortex flowfield for a highly flexible aeroelastic UH-60A rotor in forward flight [11] is repeated here. The experimental wake data were acquired using Particle Image Velocimetry (PIV) [12] during a test of the full-scale UH-60A rotor in the National Full-Scale Aerodynamics Complex 40- by 80-Foot Wind Tunnel. The PIV measurements were made in a stationary crossflow plane at 90 deg rotor azimuth. The CFD simulation was performed using the OVERFLOW CFD solver loosely coupled with the rotorcraft comprehensive code CAMRAD II for the configuration that includes experimental setup in the tunnel with Large Rotor Test Apparatus (LRTA) and support structure. Figure 8 shows the experimental setup.

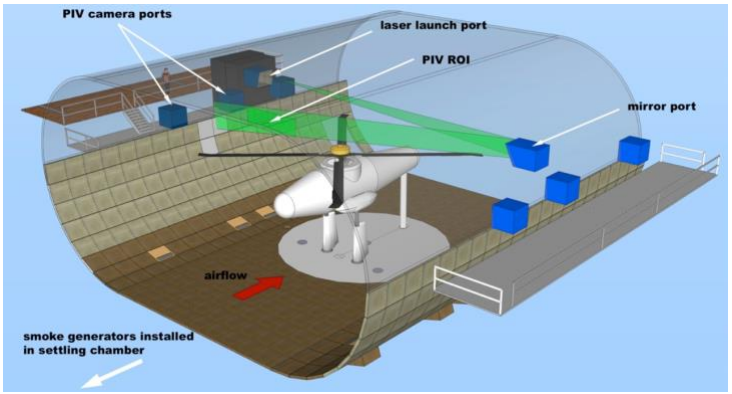


Figure 8. PIV system in the 40 by 80-ft Wind Tunnel for UH-60A Airloads test [12].

In Ref [13], characteristics of vortices captured in the PIV plane from different blades are compared with CFD calculations. Besides, the blade airloads were also calculated. Here we

compare the rotor-fuselage interactional loads. Figure 9 compares the disk model computation to the calculation of the full rotor with a moving grid at the fuselage crown line and fuselage sideline. The pressures for both computations match well for the most part except overprediction for the disk model at the dome. This is probably due to the inherent limitations of two-dimensional assumptions for the airfoil sections in BET. The unsteady pressure loads are averaged over two rotor revolutions in the case of full rotor simulations and equivalent number of iterations in case of steady state disk model. Figure 10 compares the tunnel floor pressure from both calculations. The unsteady variation is evident near rotor and LRTA center. The variations in the rest of the location along the line is minimal. This pressure was also represented as an average of two rotor revolutions for full rotor case and few steady state iterations.

5. 3 Generic rotorcraft fuselages (ROBIN)

Figure 11 shows flow simulation for a rotorcraft fuselage that is typically designed with an emphasis on operational functionality [13]. The NASA Rotary Wing Project has conducted both experimental and computational investigations to assess active flow control as an enabling technology for fuselage drag reduction. That study evaluated numerical simulations of a flow control system on a generic rotorcraft fuselage (ROBIN-mod7) with a rotor in forward flight using OVERFLOW [13]. The results are compared to fuselage forces, surface pressures, and PIV flow field data obtained in a wind tunnel experiment conducted at the NASA Langley 14-by 22-Foot Subsonic Tunnel, where significant drag and download reductions were demonstrated using flow control.

Pressures were compared at the ramp for a baseline case. Computations were carried out with OVERFLOW full rotor unsteady moving grid and disk model. Both models over predict the backpressure in the middle of the ramp for the baseline case [13], Figs. 11(b). Ref. [13] uses two different turbulent models. The experiment shows a flat pressure region as on the bottom of the ramp centerline, where the SA and SST models over-predict these pressures. While the SST model shows better agreement with the experiment than the SA model, there are considerable differences between SST results and the experimental data on the ramp. Fig. 11(c) shows pressure at the centerline of the fuselage. The lower centerline nose pressure is predicted very well for the full rotor simulation, but the disk model over predicts. This configuration shows a decrease in the suction peaks at the bottom of the ramp for both the SA and SST turbulence models. Ref [13] mentioned that this is also a region where it is expected that the CFD will match the experiment and is a good check on how well the CFD is modeling the correct flow conditions, fuselage AoA, and rotor downwash. The Cp values at the aft of nose does not match well with the experimental data very well for both disk model as well as full rotor.

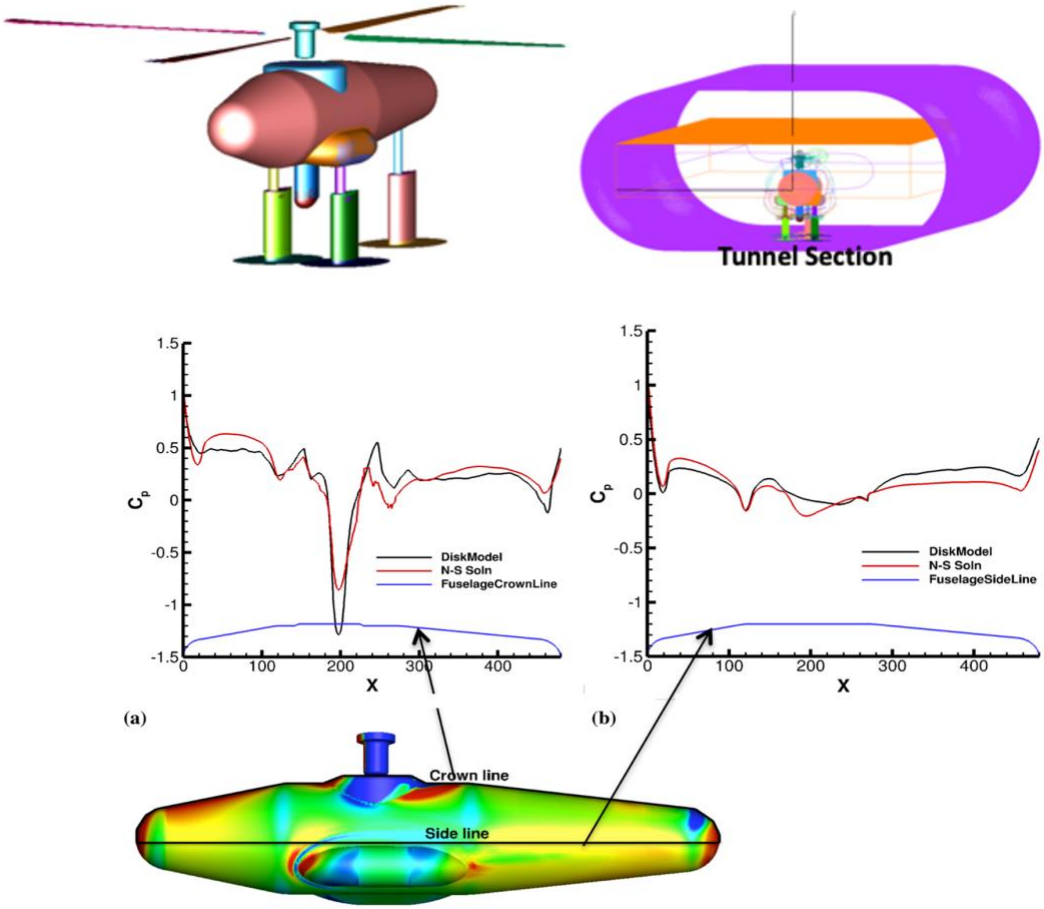


Figure 9. UH-60 in forward flight Run 73, Advance-ratio = 0.15. (a). Cp on the fuselage crown OML. (b). Cp on the fuselage side OML. Comparison of pressure on the fuselage crown line and sideline.

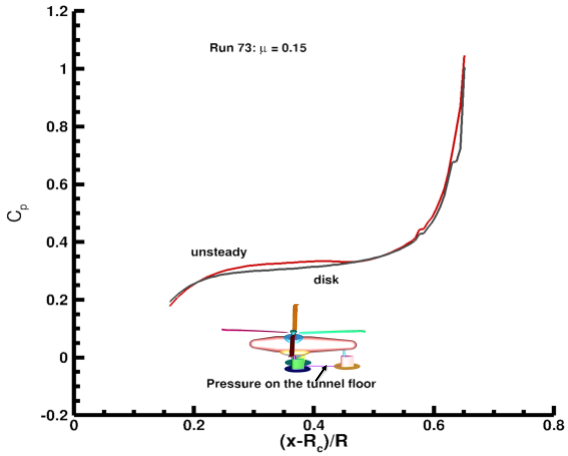


Figure 10. Comparison of tunnel floor pressure between fully modeled rotor blades and rotor disk model.

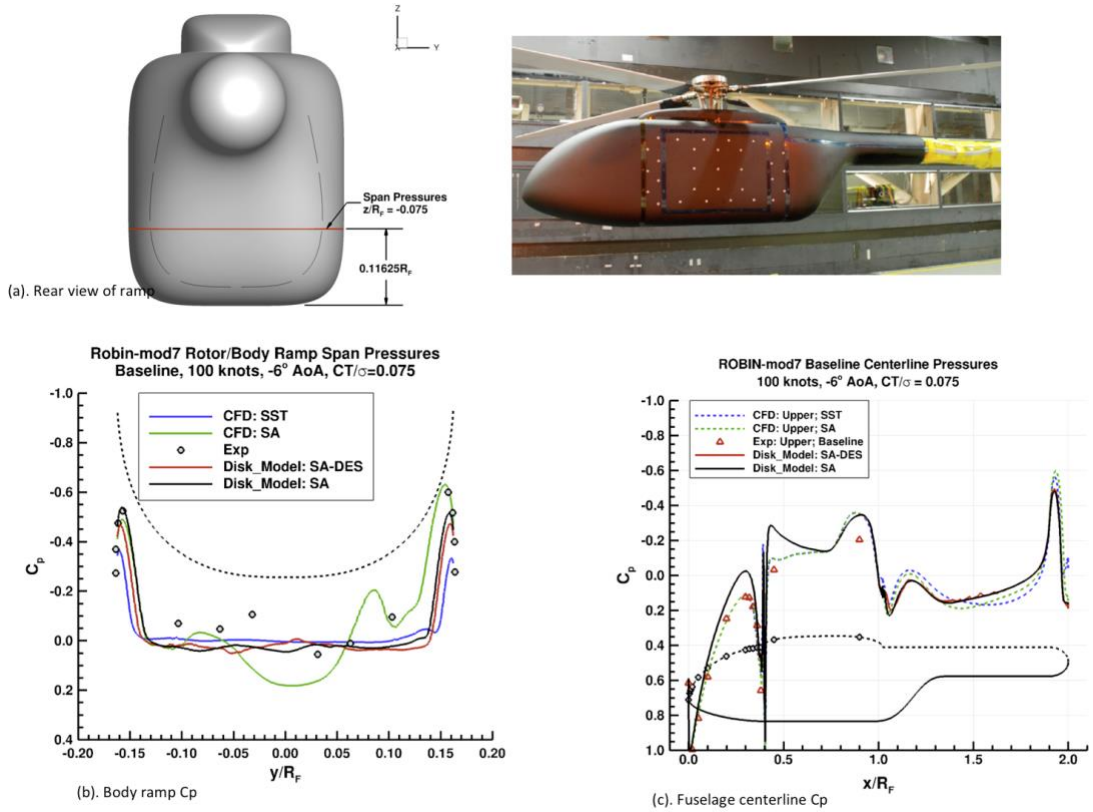


Figure 11. Spanwise Cp profile comparison CFD (full rotor unsteady), disk model, and experiment, $AoA = 6°, \mu = 0.25, \frac{C_T}{\sigma}$ = 0.075 [13].

5. 4 Concept Vehicle: Coaxial rotor

Next, we presented some computations for newly established concept vehicles [14-15]. Concept vehicles are developed for air taxi operations, also known as urban air mobility or on-demand mobility applications. These concept vehicles are intended to focus and guide NASA research activities in support of aircraft development for emerging aviation markets, in particular, VTOL air taxi operations. One such concept vehicle is the low-emission coaxial rotor. Flows for this coaxial case with both full rotors unsteady moving grid and disk model of OVERFLOW/CAMRAD II loosely coupled interface is computed.

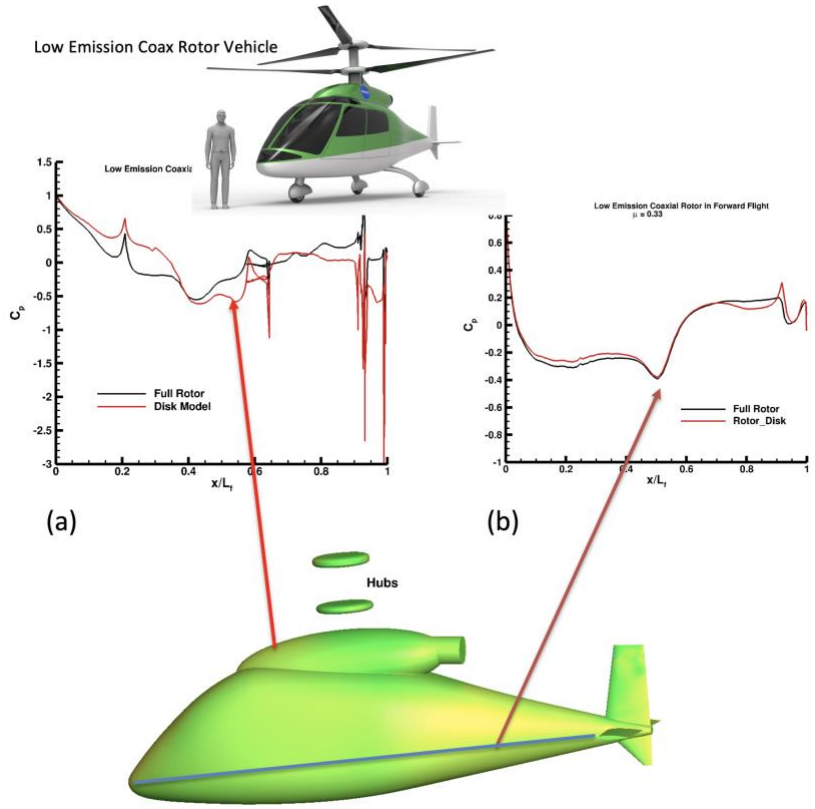


Figure 12. Low emission conceptual vehicle: Coaxial Rotor in Forward flight [12]. Cp from Rotor-Disk Model (target thrust and torque balanced). Top: shows vehicle drawing. (a) Crown line, (b) Midline. Bottom: shows the surface pressure on the vehicle including the hubs (Disk model).

Figure 12 shows the pressure variations on the fuselage, which shows one aspect of the interactional aerodynamics due to the rotor. The full rotor unsteady simulation was done with CAMRAD II coupled OVERFLOW. The simulation with rotor disk was performed without CAMRAD II coupling. The average pressure distribution in the symmetry plane of the fuselage for different rotor azimuth angles and for two rotor revolutions. The rotor downwash impinging on the upper side of the fuselage during a blade passage, especially the lower rotor leads to a pressure rise on the upper side of the fuselage. There is a peak in the pressure distribution at the hub/dome location. The bigger pressure peaks occur near the rear end of the fuselage at the vertical tail. Similarly, there are pressure peaks in the midline outer mold line (OML). The pressure peak at the horizontal tail is not as prominent as vertical tail. These pressure variations in general are higher for the disk model prediction which could be due to some of inherent limitation of BET as mentioned in [2], especially, the full 3-D effects.

5. 6 Concept Vehicle: Lift+Cruise

The next simulation is on a concept vehicle configuration of Lift+Cruise. The lift+cruise type of aircraft is intended to represent a class of VTOL aircraft which have been developed recently. Silva et al [15] provided a detailed description of this vehicle. This vehicle can operate manned and unmanned and takes advantage of distributed electric propulsion. The lift+cruise vehicle is intended to work as a fixed-wing aircraft whenever possible and run the VTOL lift rotors only during the VTOL phases of flight. The most distinctive attribute of these concepts is that the rotors for lift are separate from those used for propulsion, and the lift rotors are not used (stopped and aligned with flow) during cruising flight. As such, the lift rotors are intended to generate small aerodynamic forces and moments during cruise. All eight rotors and propulsor at the back are

shown with the rotor numbers. Figure 13 helps in the rotor arrangement and rotor numbering. The right figure shows the contour of normal forces on the rotor plane for the pusher propellor in transition flight. Figure 14 shows the contour of normal force distribution in disk for rotors. Figure 15 shows the loose coupling convergence (also referred to as delta coupling) for this transition flight. To verify that at convergence, the aerodynamic load predicted by CAMRAD II's aerodynamic models approaches the CFD computed airloads, the delta load for the interface were calculated. This delta formed at the CAMRAD II's collocation points, which are usually coarser than the CFD data points. In Figure 16, we show some flow visualizations for Lift+Cruise configuration in hover. Finally, Figure 17 presents hover coupling convergence like Figure 15 for transition flight. This oscillatory convergence at the propellor in case of transition flight is due the high impact of the wake from the front rotors. The oscillatory convergence for the hover simulation indicated that simulation needed to continue for several rotor revolutions.

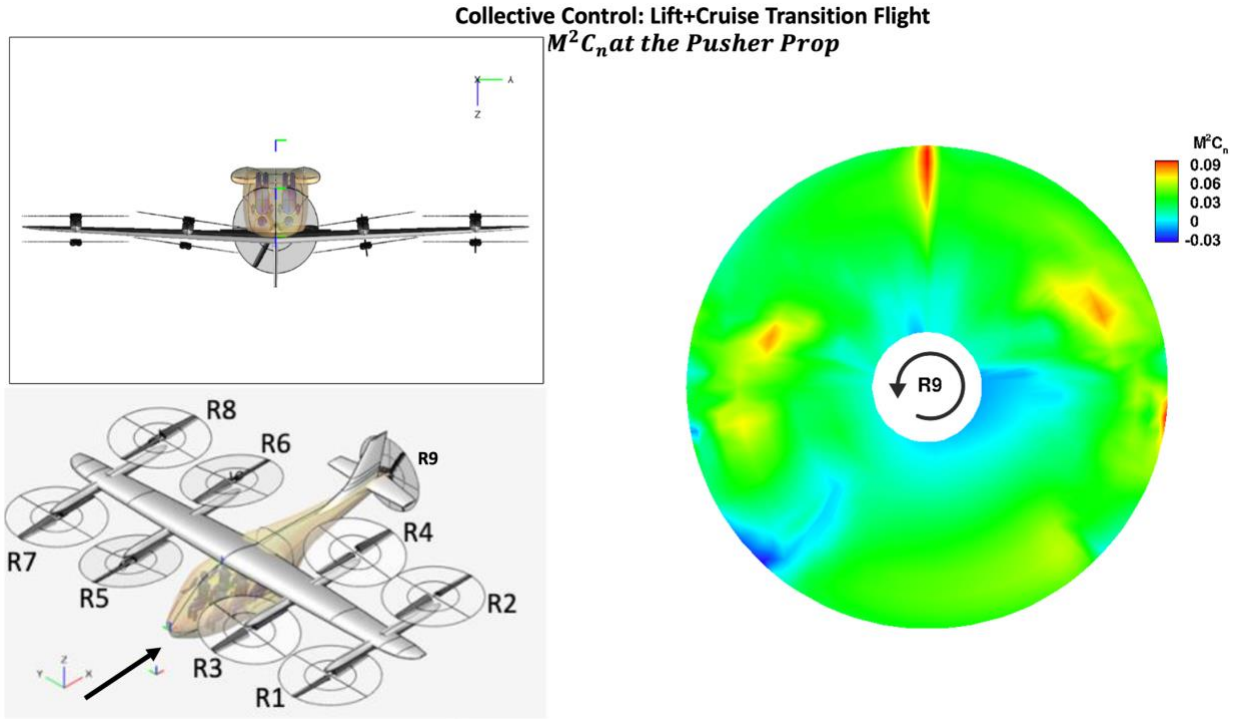


Figure 13. Left: the rotor orientation and rotor identification numbering. Right: Rotor 9, M^2C_n on the disk plane for Lift+Cruise conceptual vehicle in transition flight, collective control

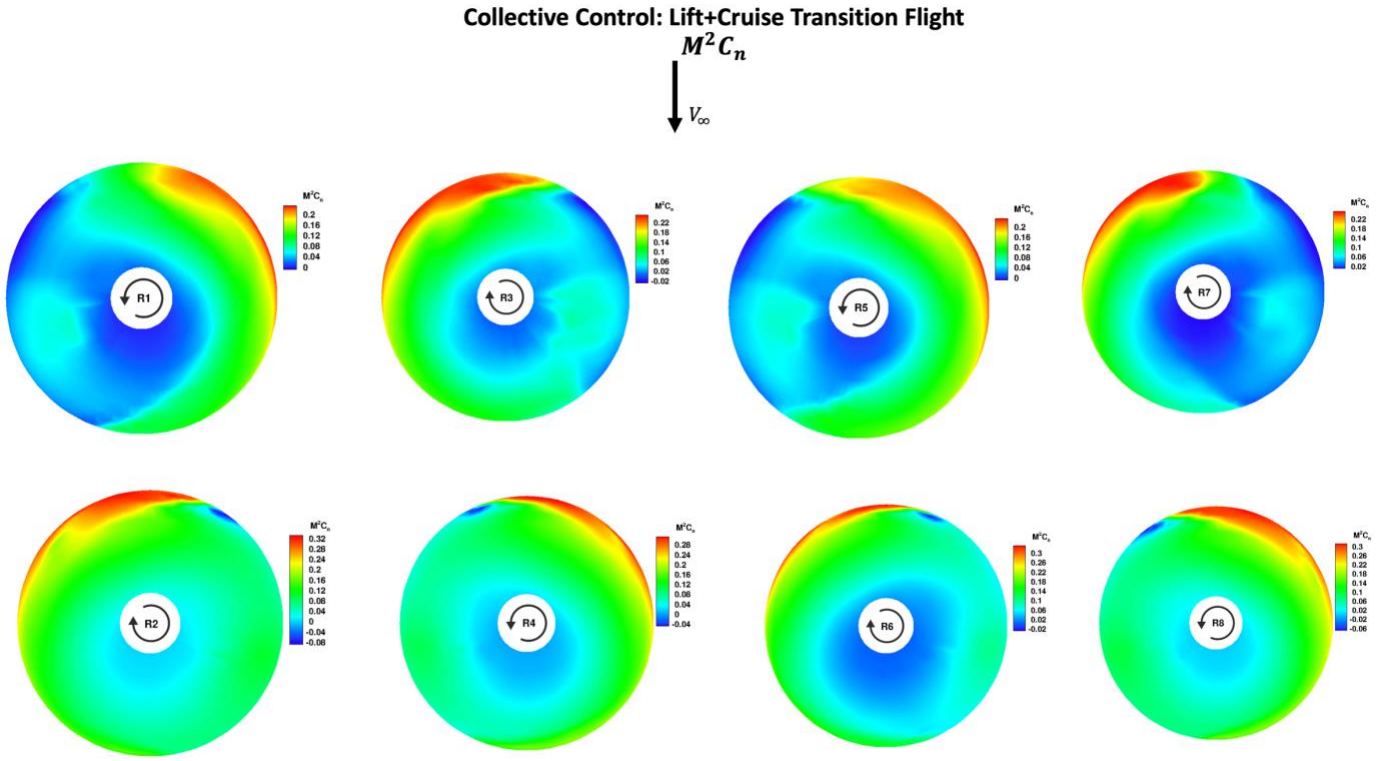


Figure 14. M^2C_n on the disk plane for Lift+Cruise conceptual vehicle in transition flight, collective control

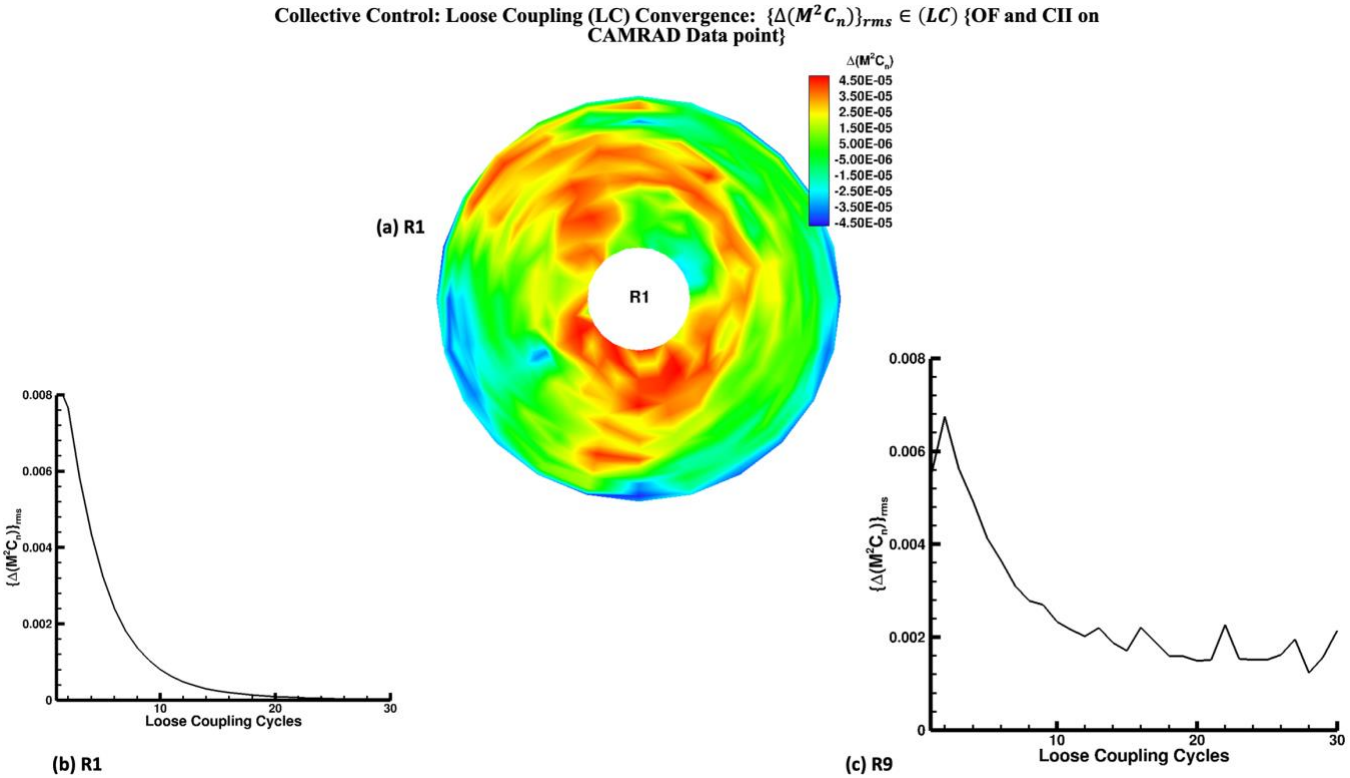


Figure 15. Loose coupling convergence between the OVERFLOW and CAMRAD interface. Front Rotor 1 and aft propellor Rotor 9.



Figure 16. Lift+Cruise conceptual vehicle in hover [14]. Top: M^2C_n convergence, bottom: iso-surface of vorticity colored by Cp.

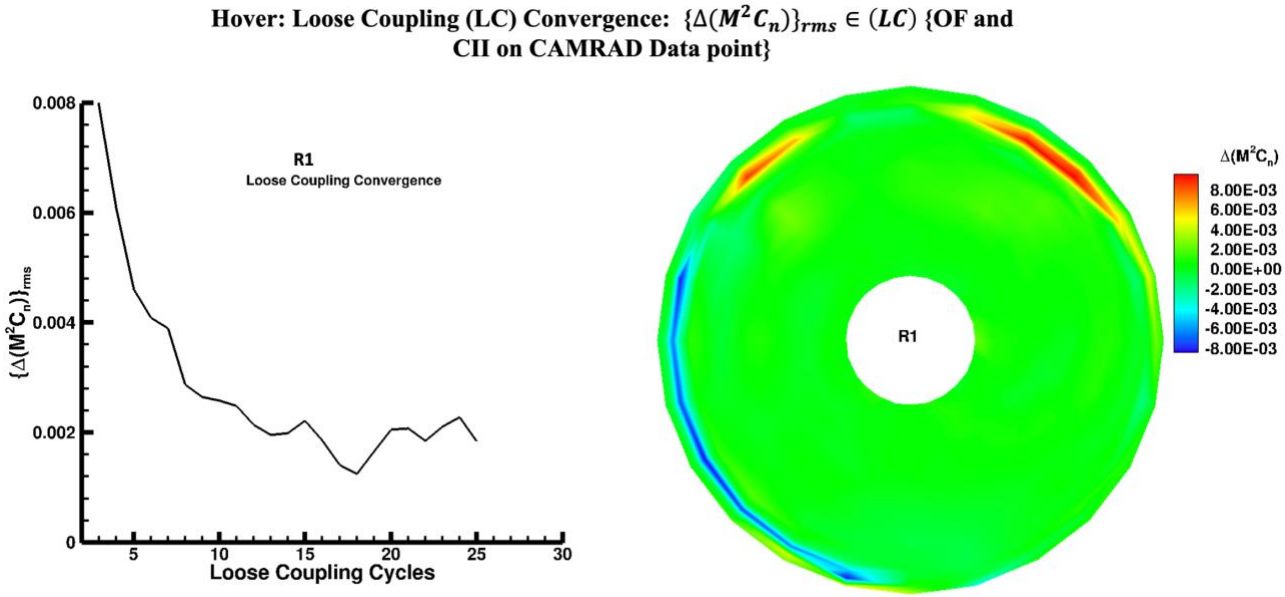


Figure 17. Loose Coupling (LC) Convergence: $\{\Delta(M^2C_n)\}_{rms} \in (LC)$ {OVERFLOW and CAMRAD II on CAMRAD Data points for hover, Rotor 1.

5. 6 UAM Vehicle in Multirotor Test Bed

The final case presented here is a multirotor experiment. NASA recently developed the Multirotor Test Bed (MTB) [16-17] system as a part of the agency's Revolutionary Vertical Lift Technology (RVLT) Project to facilitate wind tunnel testing for new and existing multirotor aircraft configurations, with a focus on collecting validation data for Urban Air Mobility vehicle simulations. The MTB is currently capable of testing up to six rotors with the potential to expand to even more than six rotors. The MTB is designed to adjust the vertical, lateral, and longitudinal placement of each rotor, as well adjust the rotor tilt and the pitch of the whole assembly. Improvements are currently being made to the MTB to improve the quality of the data measurements for future MTB testing scheduled to take place in 2022.

A detailed description of the experiment of the Multirotor Test Bed (MTB) project is given in Refs. [16-17]. Figure 18 shows the MTB as it was tested in the U.S. Army 7- by 10- Foot Wind Tunnel at NASA Ames. The MTB has the flexibility to test larger-scale rotor configurations when compared to previous tests using small hobby-scale UAS. This allows for testing at rotor tip Reynolds numbers more relevant to full-scale piloted electric vertical take-off and landing (eVTOL) aircraft expected for UAM operations. The experiment allows the multirotor design space to be parametrically explored. By measuring individual rotor loads for a multirotor system and allowing for adjustments to individual rotor position and tilt angle. Each rotor can tilt forward 90 deg and backward 5 deg. In addition, the entire MTB can tilt forward 20 deg and backward 10 deg through the central support structure, known as the strongback. The strongback is the backbone of the support structure assembly. The flexibility of the strongback assembly allows the entire multi-rotor system to be tested in many different multirotor and tilting-rotor configurations. The rotors can be arranged in tall and short configurations height-wise via adjustable support arms. The CFD simulations will be validated for the multirotor configurations in hover and edgewise forward flight for short configurations.

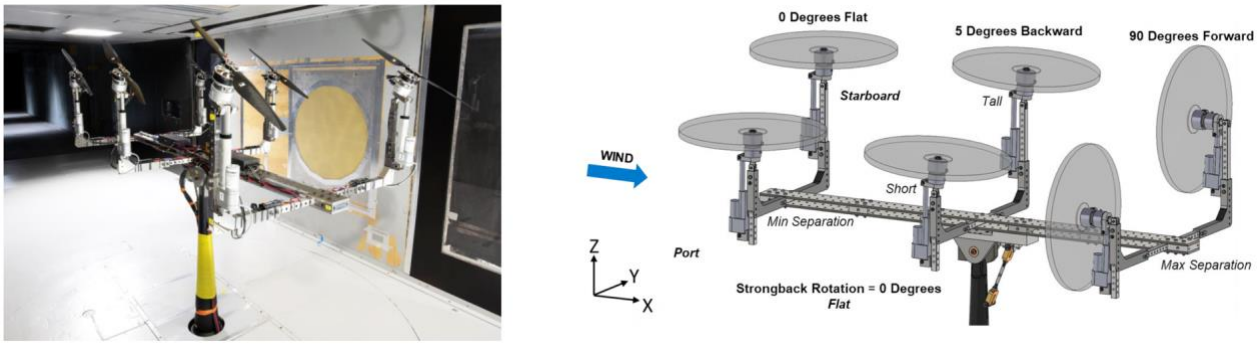


Figure 18. MTB in the U.S. Army's 7-by 10-Foot Wind Tunnel at NASA Ames Research Center[1,2]. Picture on the right shows the tall and short configuration of the rotor support arms.

The MTB six-rotor case with the rotor-disk model is shown first in Figures 19-23. Two studies were performed for the MTB's short rotor configuration for wind tunnel speeds of 20 ft/s and 40 ft/s. Figure 19-21 qualitatively compares the normal force for all the rotor disks. The two varying fidelity simulations seem to be close to each other with slight changes in the magnitude and phases. In general, the disk model predicts a higher normal load throughout the greater quadrant on the advancing side. Nevertheless, the similarity between these two varying fidelities is encouraging. Figure 22 shows the two cases of six-rotor trimmed solutions and comparisons to the experiment. The figure on the left is -5 deg MTB pitch, while the figure on the right is 0 deg pitch MTB assembly and at a tunnel speed of 40 ft/sec. For these results, only three longitudinal rotors on one side, right side, (or y+ side, starboard side), namely, R1, R3, and R5 were trimmed, whereas in Figure 9(b) in the sensitivity study section, the trimming was performed for the left side (y- side, port side) rotors, R2, R4, R6. The computation preserves the lateral symmetry while the measured data show asymmetry. Figure 22 shows the convergence of the loosely coupled solution for the two front rotors. All the rotors behave similarly, so for conciseness, we presented one clockwise rotor (Rotor 2) and one counterclockwise rotor (Rotor 1). CII in these figures refers to comprehensive code CAMRADII while OF is referred to as OVERFLOW. At the OF and CII interface, the load is transferred through a delta module at CII collocation points. This is done in general because a higher resolution requirement on the comprehensive side is not needed as opposed to the CFD level. At 'loose coupling (LC)' convergence, this delta load should approach zero. The two plots on the left of Fig. 12(a-b) are the normal loads for OF and CII at the CII collocation points. They are close to each other at convergence. The right figures show the value of delta loads and L2-norm of delta load.

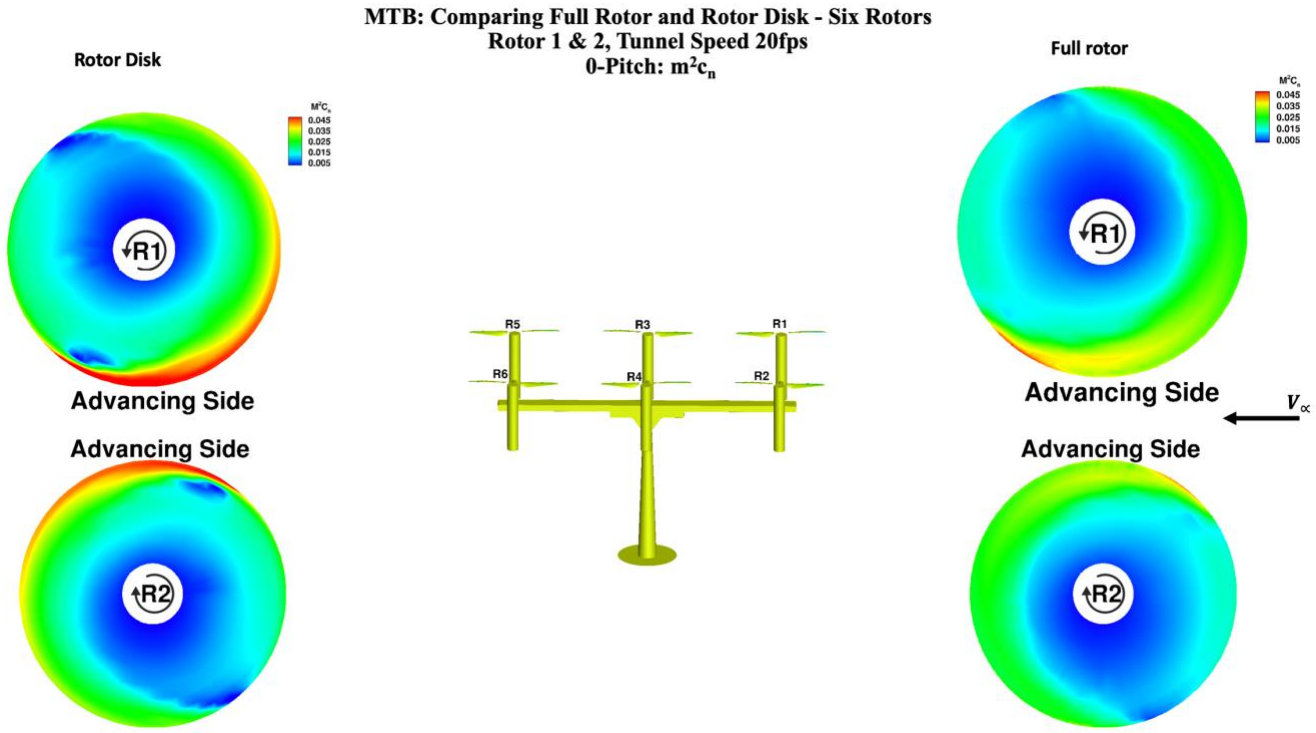


Figure 19. MTB: M^2C_n on the disk plane for the two front rotors, R1 and R2 for the six rotors configuration. The figure in the left shows the rotor-disk and the right shows the full rotor results.

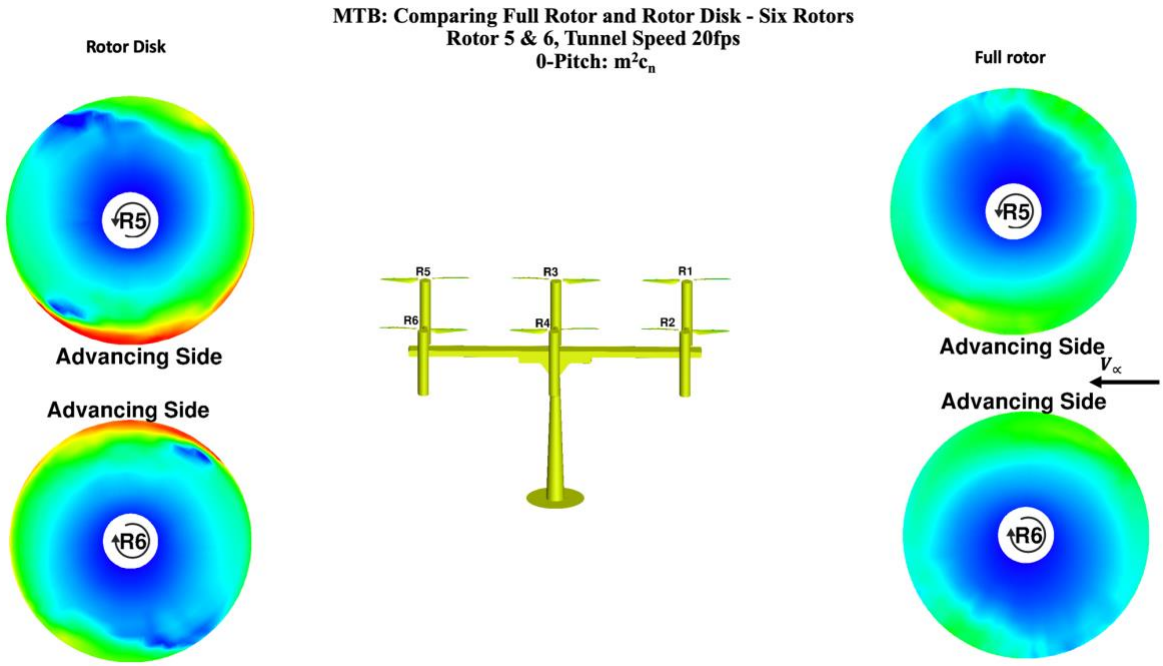


Figure 20. MTB: M^2C_n on the disk plane for the middle two rotors, R3 and R4 for the six rotors configuration. The figure in the left shows the rotor-disk and the right shows the full rotor results.

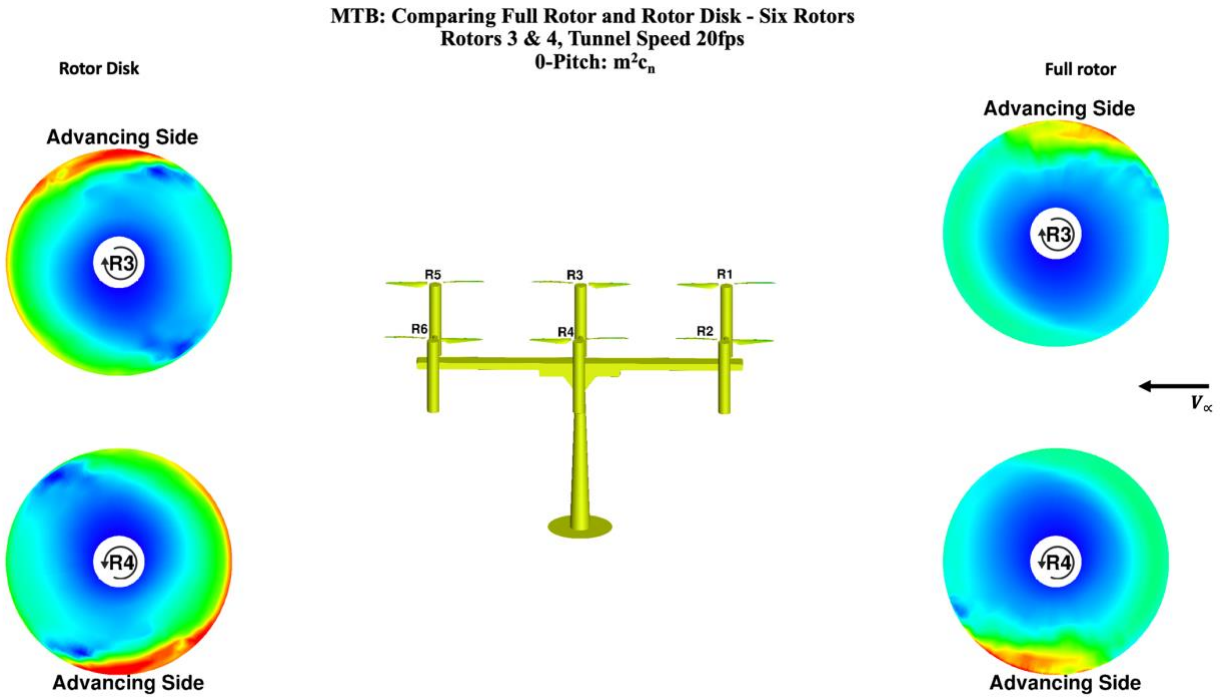


Figure 21. MTB: M^2C_n on the disk plane for the two middle rotors, R5 and R6 for the six rotors configuration. The figure in the left shows the rotor-disk and the right shows the full rotor results.

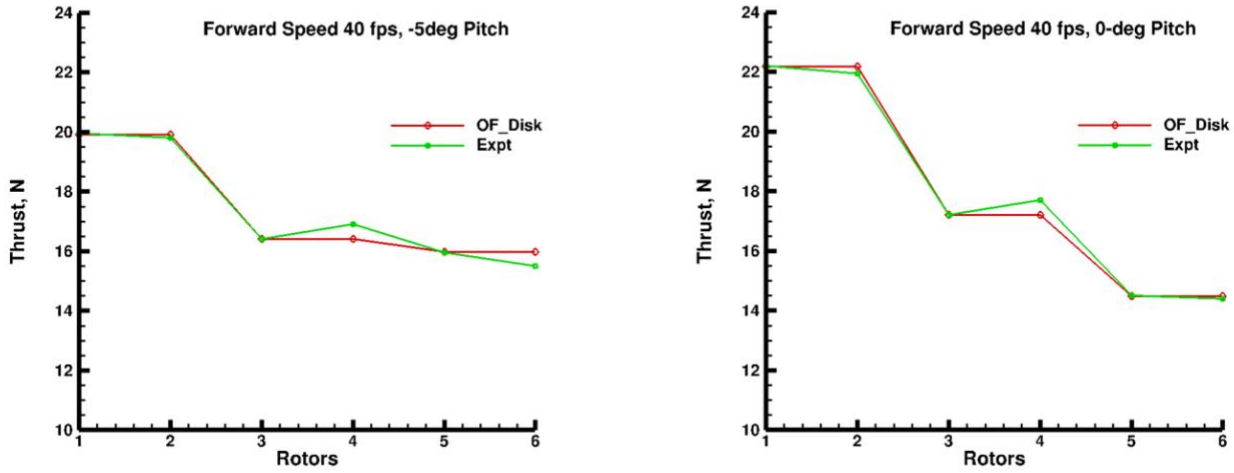
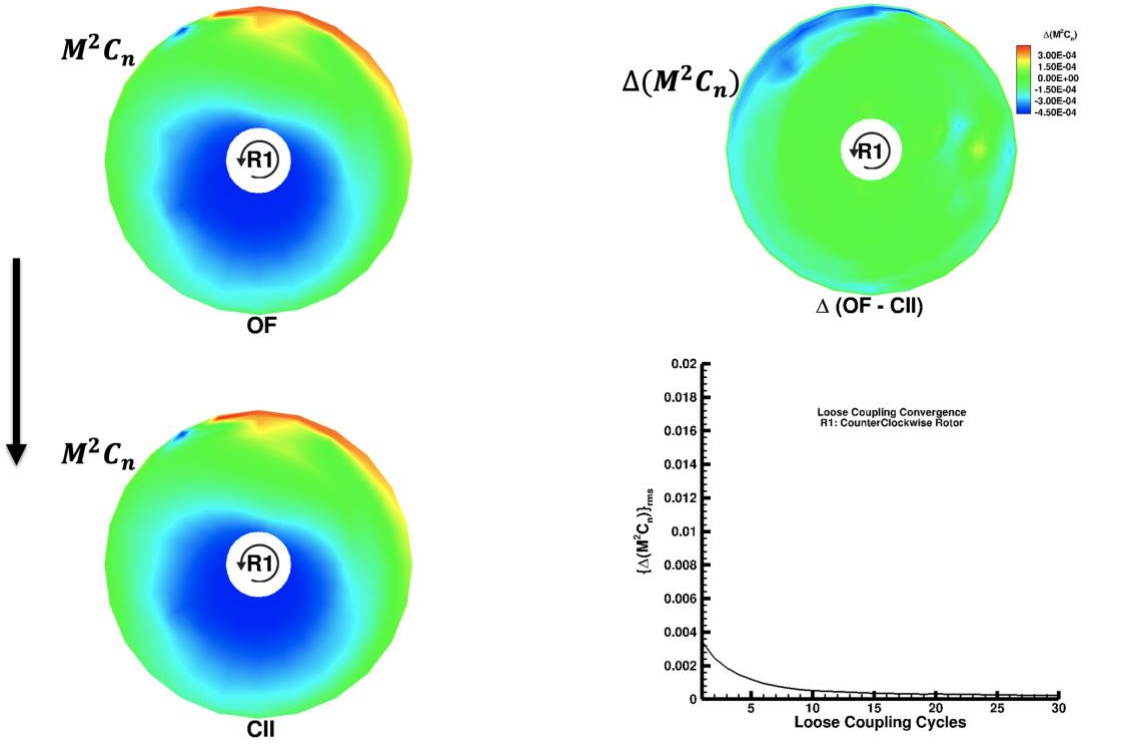
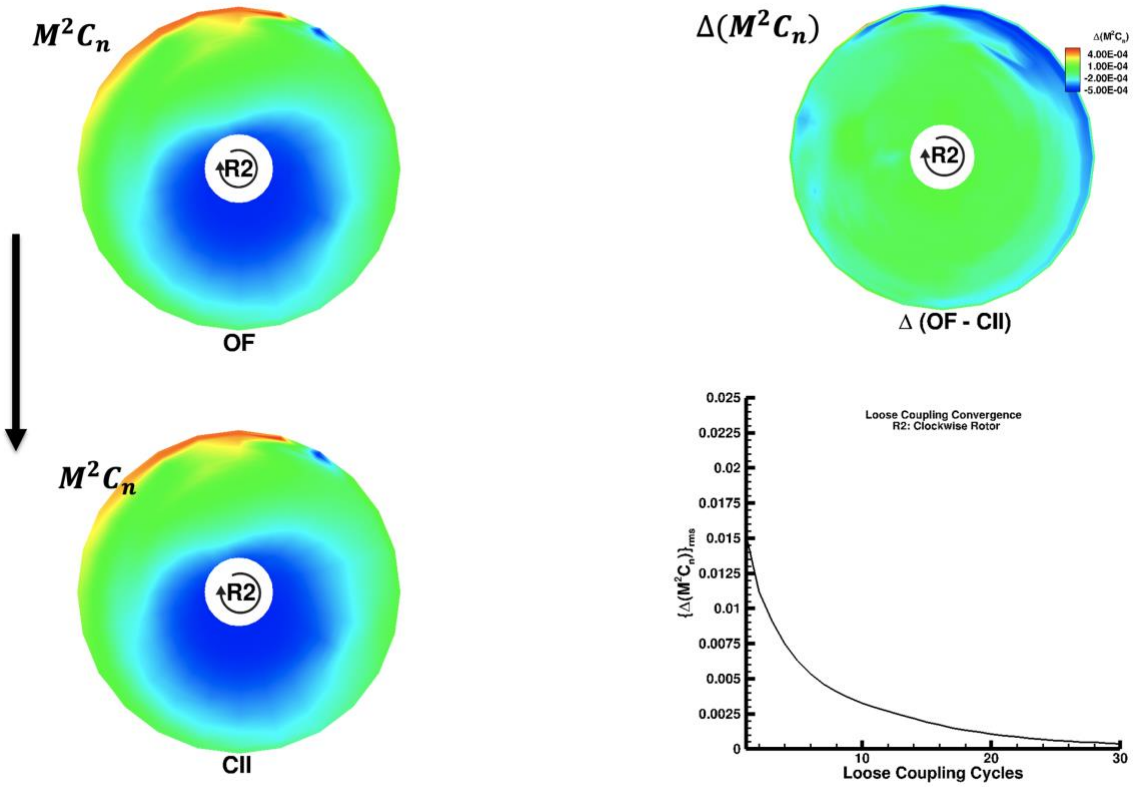


Figure 22. MTB 6 rotors: Comparing Rotor-Disk model trimmed solution to the experiment.



(a) R1



(b) R2

Figure 23. Loose Coupling (LC) Convergence for R1 and R2: $\{\Delta(M^2C_n)\}_{rms} \in (LC)$\{OF and CII on CAMRAD Data point\}. Left two figures in (a) and (b) show the normal load at the CAMRAD

collocated points. Right two figures show the delta load convergence between OVERFLOW and CAMRAD II.

6. Summary

Application and development of a rotor disk model in Overflow is presented. The development includes the CFD OVERFLOW code loosely coupled with the CAMRAD II comprehensive code. The OVERFLOW/CAMRAD coupling is well established for rotor flows using unsteady moving blades with overset grids. The rotor disk model coupling is recently established, and the procedure is described in detail including the rotor trim algorithm. Coupling the overall rotor-disk model in OVERFLOW is briefly discussed. The application of the rotor-disk model along with the trim algorithm shows the advantages for multirotor configurations. The full rotor computations of typical MTB six rotors case take about five to six days of wall clock time, while the disk model steady-state computations take about a day wall clock time. The simulations were done with about 720 cores of Intel Broadwell node at Pleaides supercomputer at NASA Ames Research Center. The typical isolated rotor case can be done in very inexpensive way. It is possible to form an aerodynamic database in reasonable timeframe.

Performed hover simulation for an isolated xv15 rotor. The performance prediction of the hover with the disk model is reasonable and promising for this widely used case.

Simulations were carried out using the Navier-Stokes equations to determine the evolutionary and dynamical characteristics of the vortex flow field for a highly flexible aeroelastic UH-60A rotor in forward flight. The disk model results are compared with the full blade simulations. The disk model shows similar trend to full rotor but consistently overpredicts at hub junctions. This is probably due to the inherent limitations of two-dimensional assumptions for the airfoil sections in BET. The pressure prediction at the floor for both methods are almost identical.

Another application of the rotor disk model for a NASA Rotary Wing Project was demonstrated. Both experimental and computational investigations assessed active flow control as an enabling technology for fuselage drag reduction. This study evaluated numerical simulations of a flow control system on a generic rotorcraft fuselage (ROBIN). The results are compared to fuselage forces, surface pressures, and PIV flow field data obtained in a wind tunnel. The pressure coefficient values for all the turbulence models for both full rotor and disk model show differences at the ramp. The Cp values on the upper surface centerline of the fuselage nose section compare well to the experimental data for both CFD turbulence models and for both full rotor and disk model. The Cp values at the aft of nose does not match well with the experimental data very well for both disk model as well as the full rotor.

Simulation of NASA concept vehicles and detailed results are presented. These concept vehicles are intended to represent a class of VTOL aircraft that have been recently developed. The first one is a low-emission coaxial rotor. The second concept vehicle is referred to as Lift+Cruise. Solution validation and convergence are demonstrated to make sure the aerodynamic loads predicted by CAMRAD II's aerodynamic models approaches the CFD computed airloads.

The final case presented is a multirotor experiment, MTB, with a focus on collecting validation data for Urban Air Mobility vehicle simulations. Both qualitative and quantitative comparisons of the computed and measured flow field reveal that the simulation captures the key features of the complex rotor wake, rotor-structure interactions, and rotor-rotor interactions. Most of the qualitative comparisons are done with fixed rotor collectives. For different collective settings, some aspects of the rotor trimming were performed with the rotor-disk algorithm.

References

1. Chaffin, M. S., & Berry, J. D. (1997). *Helicopter Fuselage Aerodynamics Under a Rotor by Navier-Stokes Simulation*. *Journal of the American Helicopter Society, 42* (3), 235-243.

2. O'Brian, D.M., *Analysis of Computational Modeling Techniques for Complete Rotorcraft Configurations*, Ph.D. Thesis, Georgia Institute of Technology, May 2006.
3. Zori, L. A., Mathur, S. R., & Rajagopalan, R. G. (1992). *Three-Dimensional Calculations of Rotor-Airframe Interaction in Forward Flight. AHS 48th Annual Forum.* Washington, D.C.
4. Rajagopalan, R. G. and Lim, C. K., "Laminar Flow Analysis of a Rotor in Hover, Journal of the American Helicopter Society, vol. 36, no. 1, pp. 12–23, 1991.
5. Chuiton, F.L., *Actuator disk modeling for helicopter rotors 28th European Rotorcraft Forum*, Bristol, UK September 2002.
6. Buning, P., OVERFLOW *2.3b*, NASA Langley Research Center, April 2020.
7. Johnson, W., *"Technology Drivers in the Development of CAMRAD II,"* American Helicopter Society Aeromechanics Specialists' Meeting, San Francisco, CA, Jan. 1994.
8. Potsdam, M., Yeo, H., and Johnson, W., *Rotor Airloads Prediction Using Loose Aerodynamic/Structural Coupling*, *Journal of Aircraft*, Vol. 43, No. 3, May-June 2006, pp. 732-742
9. Felker; F. F., Betzina, M. D., and Signor, D. B., *Performance and Loads Data from a Hover Test of a Full-Scale XV-15 Rotor*. NASA TM 86833, pp. 1–94, 1985.
10. Johnson, W.: *CAMRAD II Comprehensive Analytical Model of Rotorcraft Aerodynamics and Dynamics.* Johnson Aeronautics, Palo Alto, CA, 2005.
11. Ahmad, J.U., Yamauchi, G.K., Kao, D.L., *Comparison of Computed and Measured Vortex Evolution for a UH-60A Rotor in Forward Flight,* AIAA-2013-3160, 31st AIAA Applied Aerodynamics Conference, 24-27 June 2013, San Diego, CA
12. Yamauchi, G. K., Wadcock, A., Johnson, W., and Ramasamy, M., *Wind Tunnel Measurements of Full-Scale UH-60A Rotor Tip Vortices*, American Helicopter Society 68th Annual Forum, Ft. Worth, TX, May 1-3, 2012.
13. Allan, B.G., Schaeffler, N.W., Jenkins, L.N., Yao, C-S., Wong, O.D., Tanner, P.E., *Active Aerodynamic Load Reduction on a Rotorcraft Fuselage with Rotor Effects – A CFD Validation Effort*, 71st AHS Forum, Virginia Beach, VA, May 5-7, 2015.
14. Silva, C.; Johnson, W.; and Solis, E., *Multidisciplinary Conceptual Design for Reduced-Emission Rotorcraft*, American Helicopter Society Technical Conference on Aeromechanics Design for Transformative Vertical Flight, San Francisco, CA, January 2018.
15. Silva, C.; Johnson, W.; Antcliff, K.R.; and Patterson, M.D., *VTOL Urban Air Mobility Concept Vehicles for Technology Development*, AIAA Paper No. 2018-3847, June 2018.
16. Russell, C. and Conley, S., *The Multirotor Test Bed – A New NASA Test Capability for Advanced VTOL Rotorcraft Configurations*, Vertical Flight Society 76th Annual Forum and Technology Display, October 6-8, 2020
17. Conley, S., Russell, C., Kallstrom, K., Koning, W., and Romander, E., *Comparing RotCFD Predictions of the Multirotor Test Bed with Experimental Results*, Vertical Flight Society 76th Annual Forum and Technology Display, October 6-8, 2020
18. Chan, W.M., *Developments in Strategies and Software Tools for Overset Structured Grid Generation and Connectivity*, AIAA paper 2011-3051, AIAA 20th Computational Fluid Dynamics Conference, Honolulu, Hawaii, June 27-30, 2011.

Appendix A: Airfoil Tables Format

A legacy standard C81 airfoil table format is used for the Airfoil properties. A sample input generation is also included in the OVERFLOW release (c81.html). The tables are broken down into three sections, one for each coefficient and are arranged as a matrix with columns corresponding to Mach number, and rows corresponding to angle of attack. There is no requirement for each section to have data for the same values of Mach number and angle of attack. The rotor codes need this information for angles of attack ranging from $-180\ to + 180$ degrees. This data can come from experiment, CFD, or both. In C81 airfoil tables the rows represent the airfoil properties at a constant angle of attack (□) and the columns represent the airfoil properties at a constant Mach number (M). If the (□, M) combination falls outside of the

table range, the airfoil properties are set equal to the closest table values. A FORTRAN segment for writing/reading C81 formatted airfoil tables is included below.

```
      CHARACTER(LEN=80) :: FILENAME,AFNAME,STRING,AFORM,BFORM
      FILENAME = ARFNAME(M)
      READ(79,89,END=100,ERR=100) STRING
      READ(STRING(1:42),91,ERR=100) AFNAME,IL(M),JL(M),ID(M),JD(M), IM(M),JM(M)
      READ(79,92,END=100,ERR=100) (XL(I,M),I=1,IL(M))
      DO 5 J = 1,JL(M)
        READ(79,93,END=100,ERR=100) AL(J,M), (CL(I,J,M),I=1,IL(M))
    5  CONTINUE
READ(79,92,END=100,ERR=100) (XD(I,M),I=1,ID(M))
DO 15 J = 1,JD(M)
       READ(79,93,END=100,ERR=100) AD(J,M), (CD(I,J,M),I=1,ID(M))
15  CONTINUE
 READ(79,92,END=100,ERR=100) (XM(I,M),I=1,IM(M))
 DO 25 J = 1,JM(M)
       READ(79,93,END=100,ERR=100) AM(J,M),(CM(I,J,M),I=1,IM(M))
25  CONTINUE
 89    FORMAT (A80)
 91    FORMAT (A30,6I2)
 92    FORMAT (7X,9F7.0)
 93    FORMAT (F7.0,9F7.0:/(7X,9F7.0))
```

Here are first few lines from a C81 table. The first line has the name of the table "0012" and the dimensions of the three force coefficient matrices. In this table, the lift coefficient is given for 11 Mach numbers and 39 angles of attack, the drag coefficient is given for 11 Mach numbers and 65 angles of attack, and the pitching moment coefficient is given for 9 Mach numbers and 49 angles of attack.

```
0012                    11391165 949
          0.     .2    .3    .4      .5     .6     .7    .75    .8     .9      1.
-180.     0.     0.    0.     0.     0.     0.     0.     0.    0.     0.      0.
-172.5  .78    .78   .78    .78    .78    .78    .78    .78   .78    .78     .78
-161.   .62    .62   .62    .62    .62    .62    .62    .62   .62    .62     .62
-147.    1.      1.    1.     1.     1.     1.     1.     1.     1.     1.      1.
-129.    1.      1.    1.     1.     1.     1.     1.     1.     1      1.      1.
-49.   -1.18  -1.18  -1.18  -1.18  -1.18  -1.18  -1.18  -1.18  -1.18  -1.18   -1.18  -1.18
-39.   -1.18  -1.18  -1.18  -1.18  -1.18  -1.18  -1.18  -1.18  -1.18  -1.18   -1.18  -1.18
-21.   -.8     -.8    -.81   -.83   -.85   -.85   -.85   -.71   -.68   -.64    -.64
```